Coherent Emission in the Vicinity of 10 THz due to Auger-Suppressed Recombination of Dirac Fermions in HgCdTe Quantum Wells

Sergey Morozov, Vladimir Rumyantsev, Maksim Zholudev, Alexander Dubinov, Vladimir Ya. Aleshkin, Vladimir Utochkin, Mikhail Fadeev, Konstantin Kudryavtsev, Nikolay Mikhailov, Sergey Dvoretskii, et al.

Suppressed Auger recombination and Terahertz stimulated emission of Dirac fermions

S.V. Morozov[1,2], V.V. Rumyantsev[1,2*], M.S. Zholudev[1,2], A.A. Dubinov[1,2], V.Ya. Aleshkin[1,2], V.V. Utochkin[1], M.A. Fadeev[1,3], K.E. Kudryavtsev[1], N.N. Mikhailov[4,5], S.A. Dvoretsky[5,6], V.I. Gavrilenko[1,2], F.Teppe[3]

The discovery of Dirac fermions in a number of 2D and 3D materials boosted the solid state research in an unprecedented way. Among the many hopes of using their exceptional physical properties, it has been argued that their reduced non-radiative losses would allow graphene to compete with quantum cascade lasers (QCL) in the race for Terahertz (THz) emitters. Unfortunately, the non-radiative Auger recombination (AR) process is still active for massless fermions in gapless graphene. However, for massive Dirac fermions, AR can be entirely suppressed below a certain threshold of the carrier's kinetic energy that depends on the non-parabolicity and the symmetry of the electron and hole dispersions. In this work, by finely tuning the band structure of HgCdTe quantum wells (QW) hosting massive Dirac fermions, we set the electronic system below this threshold and demonstrate that the carrier recombination is purely radiative. A coherent inter-band emission reaching 9.6 THz, that is to say outside the spectral range of current QCLs, is measured under these conditions, opening the way to lossless inter-band THz emitters.

[1] Institute for Physics of Microstructures of RAS, Nizhny Novgorod, Russia, 603950
[2] Lobachevsky University of Nizhny Novgorod, Nizhny Novgorod, Russia, 603950
[3] Université de Montpellier, Laboratoire Charles Coulumb, Montpellier, France
[4] Institute of Semiconductor Physics, Siberian Branch of Russian Academy of Sciences, Novosibirsk, Russia, 630090
[5] Novosibirsk State University, Novosibirsk, Russia, 630090
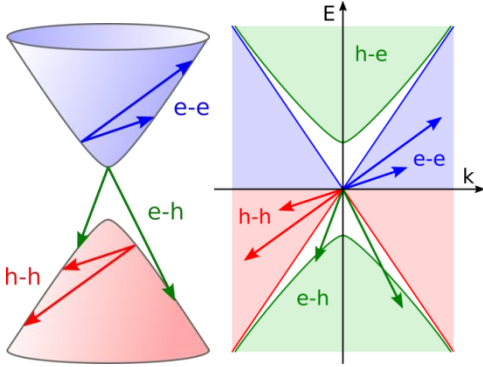[6] Tomsk State University, Tomsk, Russia, 634050

*rumyantsev@ipmras.ru

After the Nobel Prize of 2010 that revealed the groundbreaking prospects of graphene[1], there has been an increasing interest in peculiar physical properties of massless quasiparticles in solids, like Dirac[2], Kane[3,4], and Weyl[5,6] fermions, recently discovered in a number of 2D and 3D materials. Aside from a wide variety of physical phenomena ranging from the high-temperature superconductivity to the topological insulators[2], it appears that Dirac fermions in solids have their strong card for the new generation of light sources as well. Being most frequently present in zero or extremely narrow-gap materials, Dirac matter is a natural choice for emitters in the terahertz (THz), the spectral region that has been tackled for decades, but in which efficient compact lasers are still in demand for spectroscopy tasks in environmental monitoring, medicine, security etc.

Unfortunately, the probability of the radiative transitions decreases for low quanta energy and therefore interband THz emission of carriers in narrow gap materials is usually hindered by much faster non-radiative processes. Despite the fact that the radiative recombination (RR) probability grows as the square n^2 of the excess carrier concentration n, increasing the carrier density to enhance the emission is counteracted by the non-radiative Auger recombination (AR). In Auger recombination, the energy of electron-hole annihilation is transferred to a third carrier and since three carriers are involved in the Auger process, its rate rises as n^3, dominating carrier lifetime at high carrier densities.

On the other hand, it is well known that relativistic dispersion provides the unique possibility to suppress Auger recombination. When electron-hole pair recombines and the released energy is taken away by the third carrier, the energy and momentum conservation laws must be fulfilled. For hyperbolic bands, it is not possible to increment the carrier momentum k and energy E in the intraband transition by the same amount as in the interband transition. In other words, the interband (e-h) and intraband (e-e, h-h) transition "vectors" cannot be collinear in the phase space (k, E), as shown in Fig. 1. When discussing the relativistic dispersion, graphene is the first to come to mind; however, despite the fact that THz gain was recently demonstrated in graphene[7-10], there is still some debate regarding the efficiency of Auger recombination for the marginal case of massless Dirac fermions[11,12].

In particular, it was suggested that carrier heating[12] and corrugation of the band spectrum[13] can compromise the suppression of AR in graphene.

Fig. 1 The suppression of Auger recombination for massive Dirac fermions. The left part of the figure shows an example of the interband (*e-h*) and intraband (*e-e*, *h-h*) carrier transitions within hyperbolic bands. The right part presents the loci of all possible interband (green areas) and intraband (red and blue areas) transitions in the phase space (*k, E*). Energy-momentum conversation laws require *e-h* vector be collinear with either *e-e* or *h-h* vector, which is not possible. No intersection occurs between the interband and the intraband transition loci, thus forbidding the AR.

There are other materials allowing one to approach graphene-like dispersion law but leave a finite gap, thus making the properties of the carrier spectrum more stable to subtle deviations. In this respect materials with small bandgaps are of particular interest. Massless charge carriers and zero or extremely narrow bandgaps are naturally obtained in semiconductor systems when band inversion is possible, like in ternary alloys PbSnSe[14], PbSbTe[15], BiSeIn[16], HgCdTe[3], or QW based on InAs/GaSb[17] or HgTe/CdHgTe[18,19] heterostructures. In this work, we explore the interband recombination of Dirac fermions in HgCdTe epitaxial structures, by THz photoluminescence (PL) and by stimulated emission measurements as well as time resolved photoconductivity measurements. Though AR suppression and THz emission can be studied in other materials with Dirac energy spectra like InAs/GaSb[20] QWs or PbSnSe(Te)[21] alloys, we choose HgCdTe since it *combines* a number of advantages in this respect:

(i) flexibility in regard to energy spectrum design and bandgap tuning with temperature;

(ii) a well-developed growth technology delivering epitaxial structures with parameters in the wide range due to a low lattice mismatch between CdTe and HgTe;

3

(iii) low defect/impurity density;

(iv) spatially direct optical transitions in QW heterostructures;

(v) direct gap at Γ point.

Structures under study were grown on GaAs (013) substrates with ZnTe and CdTe buffers[22] using molecular beam epitaxy (MBE) with *in situ* ellipsometric control of the layer composition and thickness[23]. This growth method has been shown to provide high-quality structures, investigated in a large number of works[3,4,24,25]. The details of the growth procedure can be found in Ref [22].

To probe the carrier density relaxation, we performed a time resolved study of the photoconductivity (PC) decay. Fig. 2(a) gives the PC kinetics measured in a 3.2-nm-wide HgTe/Cd$_{0.6}$Hg$_{0.4}$Te QW (structure S1) after exciting the PC with a short (7 ns) pulse of radiation at 8.5 µm. The PC curve is strongly non-exponential, since the carrier density generated by the pumping pulse is much higher than the dark concentration of carriers as it is revealed below. The non-exponential portion of dynamics can be shown to be entirely due to RR in a very simple way.
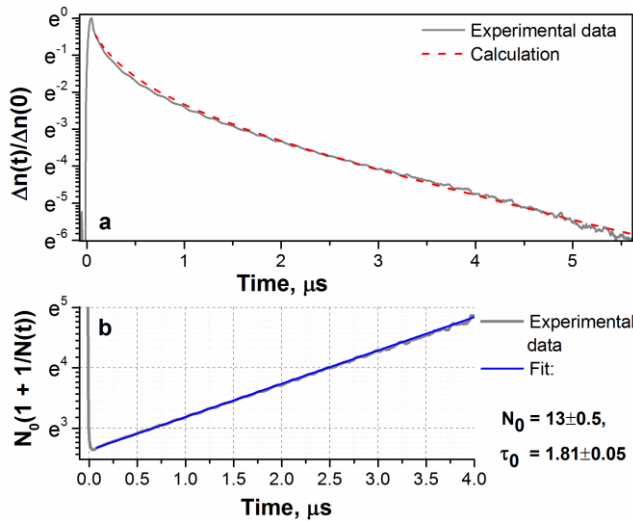
Fig. 2 a The dynamics of the carrier density in structure S1 at 77K. The vertical axis is in natural logarithmic scale. The dashed line gives the calculated kinetics for RR with the initial carrier density 1.5×10^{11} cm^{-2}. **b** The reciprocal function of the experimental data with the offset subtracted and the corresponding exponential fit.

Basically, the RR lifetime is inversely proportional to the carrier density[26]:

$$\tau_{RR} = \frac{B}{(n_0 + p_0 + \Delta n)},$$

where n_0, p_0 are the equilibrium concentrations for electrons and holes, respectively, and Δn is the excess carrier density generated by the optical excitation. Solving the equation of carrier concentration dynamics after the excitation pulse has elapsed

$$\frac{dn}{dt} = -\frac{\Delta n}{\tau_{RR}},$$

one yields the solution

$$\Delta n(t) = \frac{\Delta n(0)(n_0 + p_0)}{\left(n_0 + p_0 + \Delta n(0)\right) \exp\left(-\frac{t}{\tau_0}\right) - \Delta n(0)},$$

where $\tau_0 = B/(n_0 + p_0)$ is the RR lifetime for the $\Delta n \ll n_0$, p_0 limit. As can be seen, in the reciprocal scale the concentration kinetics is expected to have a simple form of an exponential function with offset. Introducing a dimensionless density N and N_0 as

$$N(t) = \frac{\Delta n(t)}{n_0 + p_0}, \qquad N_0 = N(0),$$

we have

$$1 + \frac{1}{N(t)} = \left(1 + \frac{1}{N_0}\right) \exp\left(-\frac{t}{\tau_0}\right).$$

Fig. 2(b) shows that the experimental data can be fit perfectly using this formula. The value N_0 provides the ratio between the initial excess carrier density and the equilibrium one. The dark carrier concentration according to Hall effect measurements lies in $(1.2 - 1.5) \times 10^9$ cm^{-2} range. Therefore the excess carrier density at t = 0 can be estimated as $(1.5 - 2) \times 10^{10}$ cm^{-2}. Using the initial carrier density of 1.5×10^{10} cm^{-2}, a rigorous calculation for the carrier density dynamics driven only by RR yields the red dashed line in Fig 1(b). Thus, owing to the specific properties of Dirac fermions one

finds no Auger-type contribution to carrier recombination in QW structure with bandgap as low as ~ 0.12 eV.

Despite the obvious advantage of AR suppression, it seems that this feature of HgCdTe QWs has remained obscure until recently. In HgCdTe, the longest lasing wavelength of 5 μm was achieved in 1993 by Aries et al[27] using bulk layers as the active region. Attempts to implement the QW structures were limited to even shorter wavelengths[28] and exploited wide QWs, in which the relativistic pattern of the carrier dispersion is not well-pronounced as shown below. Soon after 1994 the studies of the interband lasing in HgCdTe have taken a back seat due to the rapid development of the QCLs. However, though the incumbent QCLs demonstrate excellent performance both in IR and THz regions, they are mainly based on A3B5 materials and therefore encounter formidable problems within the *Reststrahlen* bands of A3B5 semiconductors[29]. In particular, QCLs[30,31] are scarce in the "gap" from 5 to 15 THz, and tunable coherent sources would be of use for spectroscopy in this region, delivering the alternative to the lead salt lasers[21,32,33]. At present, the progress in molecular beam epitaxy (MBE) made it possible to reconsider HgCdTe based structures for THz optoelectronics[24]. Stimulated emission at wavelengths of up to 20 μm was achieved in HgCdTe QWs during several past years[34] and recently gapless HgCdTe bulk crystals has been proposed for Landau level laser operating in the THz range due to suppressed Auger scattering under magnetic field[35].

Owing to lower optical phonon frequencies[36], HgCdTe allows furthering the radiation wavelength to the spectral region challenging for QCLs based on GaAs and InP[29]. In this work, we targeted the 10 – 15 THz range, and especially the wavelength of 32 μm that corresponds to the high-frequency edge of the GaAs *Reststrahlen* band and has not yet been achieved in any QCL. Note that while the proximity of GaAs *Reststrahlen* band is a problem for QCLs, we exploit it to localize the radiation in the vicinity of the active medium. Effective light confinement is a well-known challenge in the long-wavelength region. For wavelengths of ~ 30 μm the required thickness of the waveguide layer approaches the limits attainable by MBE. In this study, instead of postgrowth waveguide forming, which might be

detrimental for such delicate material as HgCdTe, we take advantage of the high reflectivity of GaAs in its *Reststrahlen* band. The latter provides the virtual metallization of the substrate when approaching 32 μm, and thus allows effective confinement of the TE mode (Fig. 3). The structures contained 5 – 10 QWs grown inside the dielectric waveguide layer so that the QWs were placed at the antinode of the TE_0 mode.
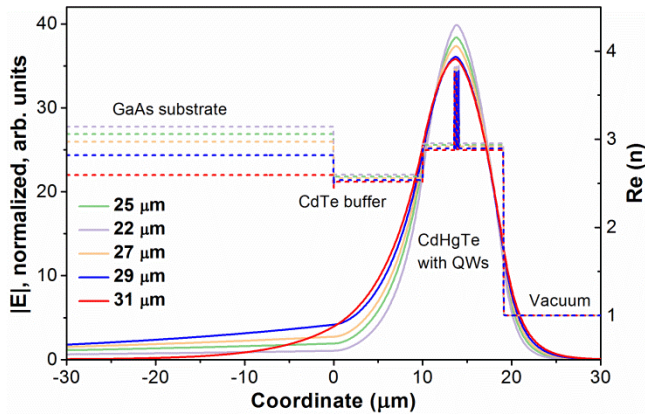
Fig. 3 The distribution of the refractive index (dashed lines) and TE_0 mode electric field (solid lines) in structure S3 for the wavelengths near 30 μm. Better confinement is evident for the wavelength of 31 μm, which is closer to the Reststrahlen band of the GaAs substrate.

The energy spectra of three HgCdTe structures having the same 40 meV bandgap are shown in Fig. 4, to understand the core idea of choosing the appropriate QW design. Kane fermions in bulk (several μm thick) narrow gap $Hg_{1-x}Cd_xTe$ include extremely low-mass electrons and light holes, while heavy holes have an effective mass of about half the mass of a free electron. When the $Hg_{1-x}Cd_xTe$ layer is shrunk down to several-nm-thick QW (with simultaneous decrease in x to keep a similar bandgap), the structure of the valence band is transformed so that a valley of low-mass holes appears at the k=0 point[19], surrounded by four side valleys hosting heavier holes[37]. As the QW width is reduced further, the valley at the k=0 point is elevated above the side maxima and becomes symmetric to the conduction band for a larger interval of carrier energy.
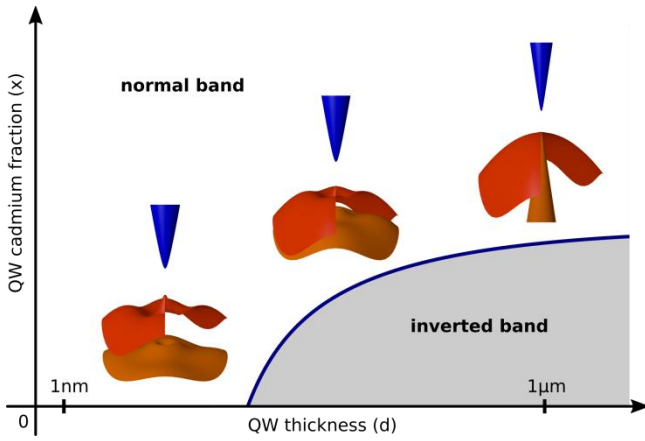
Fig. 4 Band structure transformation in narrow gap HgCdTe layer sandwiched between $Cd_{0.7}Hg_{0.3}Te$ barriers as the thickness of the layer is reduced from several microns to several nanometers.

In the general case, the net kinetic energy of the three carriers must exceed a certain threshold value for the Auger process to be allowed by the conservation laws[26,38]. The origin of this threshold can be easily understood. A relatively high energy $\sim E_g$ is released when the electron-hole pair annihilates. Therefore, the remaining electron (or hole) in the final state has a large enough momentum to carry such energy. The net kinetic energy in the initial state is a positive definite function of momentum, and the initial net momentum has to be equal to that in the final state. Thus, the kinetic energy cannot be arbitrary low, i.e. it becomes lower bounded by the value called the threshold energy. For two parabolic bands characterized by the effective masses m_1 and m_2, the threshold can be calculated analytically as

$$E_{th} = \frac{m_1 E_g}{m_1 + m_2}$$

where m_1 corresponds to the carrier taking the energy away in the Auger process[38]. One can see that in this approximation the maximum value of the AR threshold, realized for the symmetric bands, is $E_g/2$. For strongly non-parabolic energy spectrum the threshold can considerably exceed the parabolic bands limit of $E_g/2$[39,40]. In the general case it should be found numerically or geometrically by plotting the loci of interband and intraband transitions in the (k, E) space, the same way as shown in Fig.1. The "threshold" configuration of the Auger process corresponds to the intersect of the areas for intraband

8

and interband transitions. From Fig. 1 one can see that there is no such intersect for the hyperbolic bands. Therefore, the threshold energy tends to be infinite for the relativistic electron-hole dispersion, offering the tantalizing possibility to completely suppress the AR.
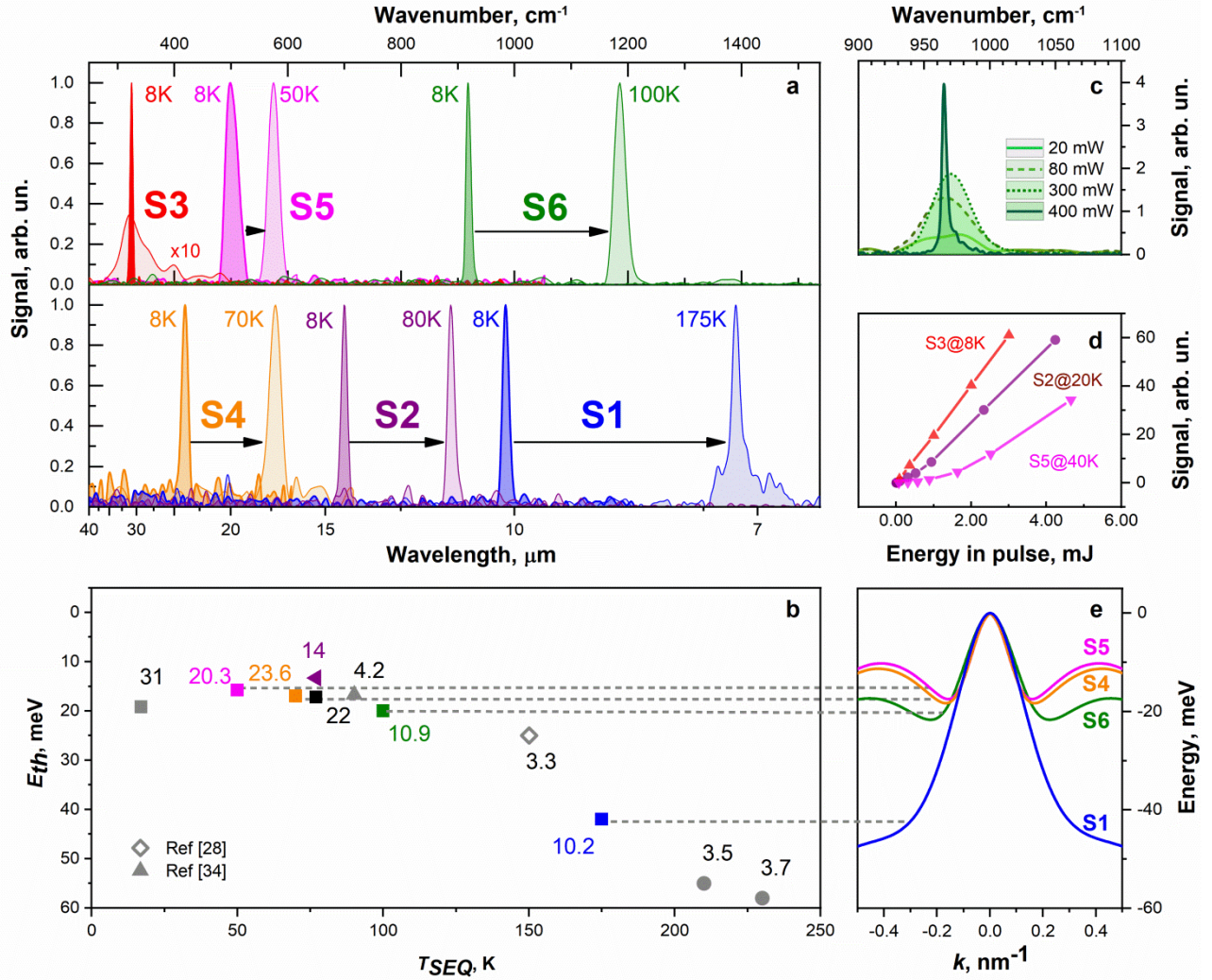
In this context, the major effect of the valence band transformation shown in Fig. 4 is the dramatic increase in the threshold energy of the AR stemming from the symmetrization and non-parabolicity of the dispersion laws in the QW. While in bulk HgCdTe heavy hole band entails miniscule AR threshold of $0.008 \times E_g = 0.25$ meV, the quasirelativistic dispersion in QWs suppresses Auger recombination completely until the hole energy is close enough to the top of the side maxima. The latter allows effectively accumulating the carriers and finally results in stimulated emission as shown in Fig. 5(a, c). The valence band flattening near the side maxima resembles the bulk material, in which the major portion of threshold energy for Auger process is introduced by the kinetic energy of the hole. Rigorous calculations of AR threshold energy demonstrate that the same holds for QW structures under study and the threshold energy is controlled by the side maxima. The dashed lines in Fig. 5(b) and Fig. 5(e) illustrate how the Auger threshold energy is built up when the side valleys are shifted downwards.

Both from experimental results and the theoretical prediction[34] it follows that the onset of stimulated emission (SE) takes place when the non-equilibrium carrier density reaches about 10^{11} cm^{-2}. Thus, the QW should be designed so that the valley at $k = 0$ could host at least this amount of "relativistic" holes. Note that the dependence of the integral SE on the pumping intensity, presented in Fig. 5(d), is well-behaved linear at 8K and tends to the (0, 0) point, i.e. the expected superlinear rise (though actually present) is extremely subtle. This is because the overwhelming majority of holes are prevented from participating in Auger recombination by their relativistic properties. As a result, before the onset of SE takes place, the recombination is still totally controlled by (spontaneous) radiative process. Therefore, the quantum efficiency of the outcome does not change significantly with the onset of SE and the latter can be detected mainly due to narrowing of the emission line, as shown in Fig. 5(c). This is quite typical for the structures under study at low temperatures. The superlinear rise becomes more evident

with increase in temperature, when high-energy holes reach the side maxima and some loss of carriers occurs via Auger recombination. Fig. 5(d) shows the corresponding examples for some of the structures under study.

There are two other factors worth mentioning here as well. The "mexican-hat" like dispersion in the valence band has a peculiar consequence of slowing down the radiative recombination at high carrier density. The holes that occupy the side valleys cannot find the electron counterpart with the same wavevector to recombine radiatively. At the same time, the side valleys have larger density of states due to larger masses of holes. The high capacity of the side valleys results in Fermi level pinning in the vicinity of their maxima as the hole density is increased. In conjunction with the onset of AR, occurring for the holes that are close to the side valleys, it ceases the possibility to obtain larger gain.

Obviously, filling the states near the side maxima that triggers the AR can be achieved not only by increasing the carrier density, but also with increase in carrier temperature. Thus, the temperature of SE quenching T_{SEQ}, i.e. the temperature above which SE cannot be obtained, becomes a sort of a probe for the threshold energy of Auger recombination. Indeed, the set of structures investigated in this work and some previous ones reveals that T_{SEQ} appears to correlate strongly with E_{th}. Fig. 5(a) shows the temperature driven spectra of SE, and Fig. 5(b) summarizes T_{SEQ} and E_{th} for a number of HgCdTe structures from several works.

Fig. 5 a Normalized temperature driven SE spectra for several structures under study. For structure S3 the PL spectrum is shown for comparison of the linewidths for PL and SE spectra; **b** The temperature of SE quenching T_{SEQ} vs. the threshold energy of Auger recombination E_{th} in HgCdTe QW structures. Labels give the longest SE wavelength obtained from the corresponding structure. The color of a dot corresponds to the energy spectrum of the same color presented in part e; **c** PL and SE spectra for structure S7 at 8K under continuous wave excitation at 900 nm. The legend gives the incident power in a 7-mm-diam spot; **d** SE integral signal vs. pumping intensity for several structures under study at different temperatures; **e** Valence band dispersion for several structures under study. The dashed lines indicate the "critical" hole energy corresponding to the threshold energy of AR.

Note that the increase in temperature broadens the bandgap in structures under study, which is a remarkable trait of narrow-gap HgCdTe. For this reason, labels in Fig. 5(b) denote the SE wavelength at 8K, i.e. the longest wavelength that was achieved for each structure. One would expect T_{SEQ} drop

with increase in the SE wavelength, mainly due to free carrier absorption. However, while the SE threshold grows with the wavelength, the change of T_{SEQ} is much weaker if the AR threshold energy is similar. Thus, a longer wavelength results in T_{SEQ} decrease only within the group with similar threshold energy. Consider the structures corresponding to 4.2 µm, 10.9 µm, 14 µm and 22 µm SE wavelengths, all having the AR threshold energy between 15 and 20 meV and T_{SEQ} in the range 80 – 100 K. At the same time, structures with similar wavelengths (consider dots at 3.5 µm, 3.7 µm vs. 3.3 µm, 10.9 µm vs. 10.2 µm, 22 µm vs. 20.3 µm) demonstrate quite different T_{SEQ} in agreement with the magnitude of the AR threshold energy.

The SE with longest wavelength of 31 µm is unto itself because the waveguide properties are also strongly temperature dependent in this case. Indeed, temperature increase of the bandgap forces the SE wavelength shift into the range where weaker TE mode localization (see Fig. 3) hinders the gain. One could expect SE to recover when the wavelength shortens down to 22 – 24 µm, but the corresponding temperature of 50 – 60 K is apparently too high to obtain SE in structure S3.

The experimental studies show that T_{SEQ} cannot be elevated by increasing the pumping intensity, indicating that gain is limited by extremely fast recombination and/or carrier heating. Both are naturally introduced by AR. Thus, the T_{SEQ} can be thought of as the temperature limit at which the Auger recombination becomes the overwhelming process controlling the dynamics of carrier distribution function.

This point is sustained by the time resolved PC measurements: the PC decay is entirely described with Auger recombination quite well (dash-dot line in Fig. 6) for structure S5 at 77K, which is well above the T_{SEQ} for this structure. Partly this is due to a low rate of RR (see dashed line in Fig. 6) that result from hole filling the side valleys, as it was mentioned earlier. To illustrate this point, Fig. 6 also gives the calculated kinetics of carrier density due to RR for a 5-nm-thick QW with the same bandgap as structure S5. Narrowing of a QW with simultaneous lowering of Cd content drives the side maxima to the lower energy and mitigates the non-monotonic "mexican-hat" pattern, the same way as for

structure S1 compared to S6 in Fig 5(c). As a result, not only the AR threshold increases, but the released holes boost RR. Thus, in narrower QWs one achieves a more favourable balance between RR and Auger processes.
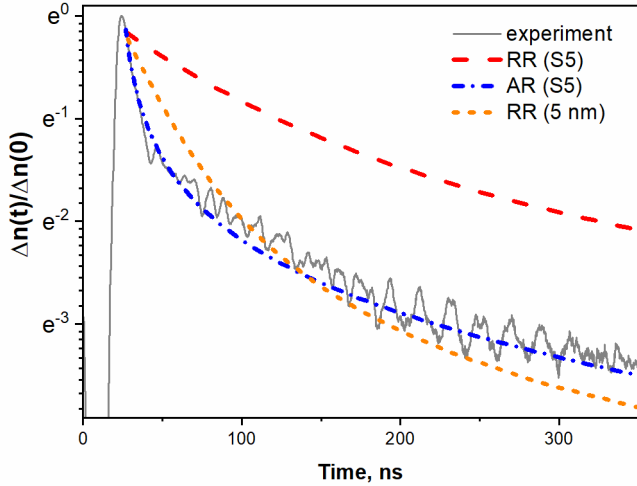
Fig. 6 The dynamics of the carrier density in structure S5 at 77K. The vertical axis is in natural logarithmic scale. The dash-dot and dashed lines give the calculated kinetics for AR and RR, respectively, for initial carrier density 8.25×10^{10} cm^{-2}. The calculated kinetics of carrier density due to RR for a 5-nm-thick QW with the same bandgap as structure S5 is given in short dash curve.

To conclude, we have demonstrated how the quasi-relativistic energy spectrum of Dirac fermions in narrow-gap HgCdTe QW structures prevents electrons and holes from recombining via Auger process, thus allowing band filling until the onset of stimulated emission takes place. Sixfold increase of the SE wavelength (from 5 to 31 μm) was achieved just by implementing relatively narrow QWs instead of bulk-like layer as the active medium. It seems that the prospects of this approach are far from being exhausted. Thoughtful designing of the band diagrams, possibly including strain engineering[41], is the basis that allows further elevating of AR threshold in QWs with even narrower bandgap. In conjunction with plasmon enhancement of THz gain[42], the AR suppression opens the opportunity to overcome two-phonon absorption in HgCdTe and go beyond 31 μm wavelength achieved in this work. In QWs with AR threshold E_{th} high enough the carrier recombination is shown to be controlled solely by the radiative mechanism, paving the way to the effective interband emitters in the THz/FIR region.

Basing on the correlation between E_{th} and the maximum operating temperature, one can hope for Peltier cooled operation of interband HgCdTe lasers with the AR threshold energy of ~ 50 meV, feasible in narrow QWs with low Cd content. Such lasers could be competitive to QCLs, scarce in 5 – 15 THz region, due to simpler structure design and the opportunity of "natural" wavelength tuning by bandgap variation with temperature.

Acknowledgements

Author Contributions

The experiment was proposed by S.V.M., V.I.G and F.T. The sample was grown by N.N.M. and S.A.D. Time-resolved photoconductivity experiments were carried out by V.V.R. and V.V.U. Photoluminescence measurements were conducted by V.V.U., M.A.F. and K.E.K. and stimulated emission measurements were performed by S.V.M., V.V.U., M.A.F and K.E.K.   Calculations of the band diagrams were done by M.S.Z. and V.Ya. A., recombination time calculations were conducted by V.Ya. A., while A.A.V. performed the electrodynamic calculation. V.V.R., V.V.U. and M.A.F. handled the data and V.V.R, M.S.Z. and A.A.V. prepared the figures. All co-authors discussed the experimental data and interpretation of the results. V.V.R., V.I.G and F.T. wrote the manuscript and all co-authors commented on it.

Competing Interests statement

The authors declare no competing interests.

References

1   Novoselov, K. S. *et al.* Two-dimensional gas of massless Dirac fermions in graphene. *Nature* **438**, 197-200, doi:10.1038/nature04233 (2005).
2   Vafek, O. & Vishwanath, A. Dirac Fermions in Solids: From High-Tc Cuprates and Graphene to Topological Insulators and Weyl Semimetals. *Annual Review of Condensed Matter Physics* **5**, 83-112, doi:10.1146/annurev-conmatphys-031113-133841 (2014).
3   Teppe, F. *et al.* Temperature-driven massless Kane fermions in HgCdTe crystals. *Nature communications* **7**, 12576, doi:10.1038/ncomms12576 (2016).
4   Orlita, M. *et al.* Observation of three-dimensional massless Kane fermions in a zinc-blende crystal. *Nat Phys* **10**, 233-238, doi:10.1038/nphys2857 (2014).
5   Jia, S., Xu, S.-Y. & Hasan, M. Z. Weyl semimetals, Fermi arcs and chiral anomalies. *Nature Materials* **15**, 1140-1144, doi:10.1038/nmat4787 (2016).
6   Xu, S.-Y. *et al.* Discovery of a Weyl fermion semimetal and topological Fermi arcs. *Science* **349**, 613-617, doi:10.1126/science.aaa9297 (2015).
7   Yadav, D. *et al.* in *Nanophotonics* Vol. 7   741 (2018).
8   Boubanga-Tombet, S. *et al.* Ultrafast carrier dynamics and terahertz emission in optically pumped graphene at room temperature. *Physical Review B* **85**, 035443, doi:10.1103/PhysRevB.85.035443 (2012).
9   Boubanga-Tombet, S. *et al.* Room-Temperature Amplification of Terahertz Radiation by Grating-Gate Graphene Structures. *Physical Review X* **10**, doi:10.1103/PhysRevX.10.031004 (2020).
10   Li, T. *et al.* Femtosecond Population Inversion and Stimulated Emission of Dense Dirac Fermions in Graphene. *Physical Review Letters* **108**, doi:10.1103/PhysRevLett.108.167401 (2012).
11   Winzer, T. & Malić, E. Impact of Auger processes on carrier dynamics in graphene. *Physical Review B* **85**, doi:10.1103/PhysRevB.85.241404 (2012).
12   Alymov, G., Vyurkov, V., Ryzhii, V., Satou, A. & Svintsov, D. Auger recombination in Dirac materials: A tangle of many-body effects. *Physical Review B* **97**, 205411, doi:10.1103/PhysRevB.97.205411 (2018).
13   Golub, L. E., Tarasenko, S. A., Entin, M. V. & Magarill, L. I. Valley separation in graphene by polarized light. *Physical Review B* **84**, doi:10.1103/PhysRevB.84.195408 (2011).
14   Dziawa, P. *et al.* Topological crystalline insulator states in Pb1–xSnxSe. *Nature Materials* **11**, 1023-1027, doi:10.1038/nmat3449 (2012).
15   Ferreira, S. O. *et al.* Experimental observation of band inversion in the PbSnTe system. *Journal of Applied Physics* **86**, 7198, doi:10.1063/1.371815 (1999).
16   Brahlek, M. *et al.* Topological-Metal to Band-Insulator Transition in(Bi1–xInx)2Se3Thin Films. *Physical Review Letters* **109**, doi:10.1103/PhysRevLett.109.186403 (2012).
17   Krishtopenko, S. S. *et al.* Massless Dirac fermions in III-V semiconductor quantum wells. *Physical Review B* **99**, doi:10.1103/PhysRevB.99.121405 (2019).
18   Bernevig, B. A., Hughes, T. L. & Zhang, S. C. Quantum spin Hall effect and topological phase transition in HgTe quantum wells. *Science* **314**, 1757-1761, doi:10.1126/science.1133734 (2006).
19   Buttner, B. *et al.* Single valley Dirac fermions in zero-gap HgTe quantum wells. *Nat Phys* **7**, 418-422, doi:10.1038/nphys1914 (2011).
20   Krishtopenko, S. S. *et al.* Temperature-dependent terahertz spectroscopy of inverted-band three-layer InAs/GaSb/InAs quantum well. *Physical Review B* **97**, 245419, doi:10.1103/PhysRevB.97.245419 (2018).
21   Maremyanin, K. V. *et al.* Terahertz Injection Lasers Based on a PbSnSe Solid Solution with an Emission Wavelength up to 50 μm and Their Application in the Magnetospectroscopy of Semiconductors. *Semiconductors* **52**, 1590-1594, doi:10.1134/s1063782618120163 (2018).
22   Mikhailov, N. N. *et al.* Growth of Hg1-xCdxTe nanostructures by molecular beam epitaxy with ellipsometric control. *International Journal of Nanotechnology* **3**, 120, doi:10.1504/ijnt.2006.008725 (2006).
23   Shvets, V. A., Mikhailov, N. N., Ikusov, D. G., Uzhakov, I. N. & Dvoretskii, S. A. Determining the Compositional Profile of HgTe/CdxHg1 – xTe Quantum Wells by Single-Wavelength Ellipsometry. *Optics and Spectroscopy* **127**, 340-346, doi:10.1134/s0030400x19080253 (2019).

24   Ruffenach, S. *et al.* HgCdTe-based heterostructures for terahertz photonics. *APL Materials* **5**, 035503, doi:10.1063/1.4977781 (2017).

25   Gusev, G. M. *et al.* Quantum Hall Effect near the Charge Neutrality Point in a Two-Dimensional Electron-Hole System. *Physical Review Letters* **104**, 166401 (2010).

26   Blakemore, J. S. *Semiconductor Statistics* (Pergamon, 1962).

27   Arias, J. M., Zandian, M., Zucca, R. & Singh, J. HgCdTe infrared diode lasers grown by MBE. *Semiconductor Science and Technology* **8**, S255 (1993).

28   Bleuse, J., Bonnet-Gamard, J., Mula, G., Magnea, N. & Jean-Louis, P. Laser emission in HgCdTe in the 2–3.5 μm range. *Journal of Crystal Growth* **197**, 529-536, doi:10.1016/S0022-0248(98)00746-5 (1999).

29   Vitiello, M. S., Scalari, G., Williams, B. & De Natale, P. Quantum cascade lasers: 20 years of challenges. *Optics express* **23**, 5167-5182, doi:10.1364/OE.23.005167 (2015).

30   Razeghi, M. *et al.* Quantum cascade lasers: from tool to product. *Optics express* **23**, 8462-8475, doi:10.1364/OE.23.008462 (2015).

31   Williams, B. S. Terahertz quantum-cascade lasers. *Nat Photon* **1**, 517-525 (2007).

32   Shotov, A. P. Tunable diode lasers for 3 to 40 μm infrared spectral region. *AIP Conference Proceedings* **240**, 87-94, doi:10.1063/1.41379 (1991).

33   Adams, A. R., Elliott, C. T., Krier, A., Murdin, B. N. & Tacke, M. Lead–salt lasers. *Philosophical Transactions of the Royal Society of London. Series A: Mathematical, Physical and Engineering Sciences* **359**, 547, doi:10.1098/rsta.2000.0742 (2001).

34   Morozov, S. V. *et al.* Long wavelength stimulated emission up to 9.5 μm from HgCdTe quantum well heterostructures. *Applied Physics Letters* **108**, 092104, doi:10.1063/1.4943087 (2016).

35   But, D. B. *et al.* Suppressed Auger scattering and tunable light emission of Landau-quantized massless Kane electrons. *Nature Photonics* **13**, 783-787, doi:10.1038/s41566-019-0496-1 (2019).

36   Talwar, D. N. & Vandevyver, M. Vibrational properties of HgCdTe system. *Journal of Applied Physics* **56**, 1601, doi:10.1063/1.334144 (1984).

37   Krishtopenko, S. S. & Teppe, F. Realistic picture of helical edge states in HgTe quantum wells. *Physical Review B* **97**, 165408, doi:10.1103/PhysRevB.97.165408 (2018).

38   Abakumov, V. N., Perel, V. I. & Yassievich, I. N. *Nonradiative Recombination in Semiconductors*. (Elsevier Science Publishers, 1991).

39   Alymov, G. *et al.* Fundamental Limits to Far-Infrared Lasing in Auger-Suppressed HgCdTe Quantum Wells. *ACS Photonics* **7**, 98-104, doi:10.1021/acsphotonics.9b01099 (2020).

40   Aleshkin, V. Y., Dubinov, A. A., Rumyantsev, V. V. & Morozov, S. V. Threshold energies of Auger recombination in HgTe/CdHgTe quantum well heterostructures with 30-70 meV bandgap. *Journal of physics. Condensed matter : an Institute of Physics journal* **31**, 425301, doi:10.1088/1361-648X/ab301a (2019).

41   Leubner, P., Lunczer, L., Brüne, C., Buhmann, H. & Molenkamp, L. W. Strain Engineering of the Band Gap of HgTe Quantum Wells Using Superlattice Virtual Substrates. *Physical Review Letters* **117**, 086403, doi:10.1103/PhysRevLett.117.086403 (2016).

42   Kapralov, K., Alymov, G., Svintsov, D. & Dubinov, A. Feasibility of surface plasmon lasing in HgTe quantum wells with population inversion. *Journal of Physics: Condensed Matter* **32**, 065301, doi:10.1088/1361-648x/ab4f33 (2019).

43   Luttinger, J. M. & Kohn, W. Motion of Electrons and Holes in Perturbed Periodic Fields. *Physical Review* **97**, 869-883, doi:10.1103/PhysRev.97.869 (1955).

44   Foreman, B. A. Elimination of spurious solutions from eight-band k× p theory. *Physical Review B* **56**, R12748-R12751, doi:10.1103/PhysRevB.56.R12748 (1997).

45   Novik, E. G. *et al.* Band structure of semimagnetic $Hg_{1-y}Mn_yTe$ quantum wells. *Physical Review B* **72**, 035321 (2005).

46   Los, J., Fasolino, A. & Catellani, A. Generalization of the k·p approach for strained layered semiconductor structures grown on high-index-planes. *Physical Review B* **53**, 4630-4648, doi:10.1103/PhysRevB.53.4630 (1996).

47   Zholudev, M. *et al.* Magnetospectroscopy of two-dimensional HgTe-based topological insulators around the critical thickness. *Physical Review B* **86**, 205420 (2012).

48   Aleshkin, V. Y. *et al.* Radiative recombination in narrow gap HgTe/CdHgTe quantum well heterostructures for laser applications. *Journal of Physics: Condensed Matter* **30**, 495301, doi:10.1088/1361-648X/aaebf5 (2018).

49   Shao, J. *et al.* Modulated photoluminescence spectroscopy with a step-scan Fourier transform infrared spectrometer. *Review of Scientific Instruments* **77**, 063104, doi:10.1063/1.2205622 (2006).

50   Rumyantsev, V. V. *et al.* Spectra and kinetics of THz photoconductivity in narrow-gap Hg1–xCdxTe (x< 0.2) epitaxial films. *Semiconductor Science and Technology* **28**, 125007, doi:10.1088/0268-1242/28/12/125007 (2013).

Methods

1.   Band diagrams calculation

The calculation method is based on the envelope function approximation[43]. The wavefunction is written as an expansion over a set functions $u_{n,0}(\mathbf{r})$ with lattice periodicity forming the Kohn-Luttinger basis:

$$\Psi = \sum_n F_n(\mathbf{r})\, u_{n,0}(\mathbf{r})$$

where coefficients $F_n(\mathbf{r})$ are smooth envelope functions. Thus, the state of the electron is described by the column vector

$$\mathbf{F}(\mathbf{r}) = \begin{pmatrix} F_1(\mathbf{r}) \\ \vdots \\ F_N(\mathbf{r}) \end{pmatrix}$$

This vector is calculated as the solution of the stationary Schrodinger equation with matrix Hamiltonian operator:

$$\mathbf{H}(\hat{\mathbf{k}}, \mathbf{r})\mathbf{F} = E\mathbf{F}$$

where quasimomentum $\hat{\mathbf{k}}$ is a differential operator:

$$\hat{\mathbf{k}} = -i\nabla$$

In bulk homogeneous sample the solution is a column of plane waves described by band index n and three-dimensional wavenumber $\mathbf{k}$:

$$\mathbf{F}_{n,\mathbf{k}}(\mathbf{r}) = \mathbf{C}_{n,\mathbf{k}}e^{i\mathbf{k}\mathbf{r}}$$

where the coefficients $\mathbf{C}_{n,\mathbf{k}}$ are the solutions of the following equation:

$$\mathbf{H_k C}_{n,\mathbf{k}} = E_{n,\mathbf{k}} \mathbf{C}_{n,\mathbf{k}}$$

In quantum wells two components of quasimomentum k_x and k_y are conserved and the envelope function vector has the following form:

$$\mathbf{F}_{n,k_x,k_y}(\mathbf{r}) = \mathbf{f}_{n,k_x,k_y}(z)\, e^{i(k_x x + k_y y)}$$

where coefficients $\mathbf{f}_{n,k_x,k_y}(z)$ are the solutions of the following equation:

$$\mathbf{H}_{k_x,k_y}\big(\hat{k}_z, z\big) \mathbf{f}_{n,k_x,k_y}(z) = E_{n,k_x,k_y} \mathbf{f}_{n,k_x,k_y}(z)$$

In our calculations we use Burt-Foreman approximation[44] for 8x8 Kane Hamiltonian[45] with parameters from Ref[45]. Since our samples are grown on the crystallographic plane (013) the Hamiltonian is modified accordingly[46,47]. The z-dependent components of the envelope functions are calculated by plane wave expansion.

The model used to calculate the radiative recombination rate is described in Ref [48], while Ref.[40] describes how the threshold energies for different Auger processes can be calculated in HgCdTe QW structures.

2. PL and SE measurements

PL spectra studies were carried out at $T = 8 - 300$ K in a closed-cycle cryostat optically connected to a Bruker Vertex 80v Fourier transform infrared (FTIR) spectrometer. The FTIR spectrometer was operated in the step scan mode. When studying PL, a continuous wave laser was used with excitation wavelength in $\lambda_{exc} = 800 - 900$ nm (Ti:sapphire laser Spectra Physics «Matisse-DR»). Excitation power was varied from 10 to 900 mW. The beam spot at the sample was ~ 3 mm in diameter.

A special modulation technique was used, which is described in Ref[49], with the laser beam mechanically chopped. The modulation frequency was chosen according to detector response time, typically lying in the 200 Hz – 2 kHz range. Depending on the spectral range of the PL or signal, one of the following detectors was used: liquid N2 cooled MCT Photovoltaic D317 (range 4800 – 850 cm^{-1}), MCT/InSb sandwich D318 (range 10000 – 600 cm^{-1}) or liquid He cooled silicon bolometer D211 (range 700 – 10 cm^{-1}). The detector signal was fed to the Stanford Research System SR560 amplifier

and then recovered by a Stanford Research System SR830 lock-in amplifier. The data acquisition by the analog-to-digital converter (ADC) of the FTIR spectrometer was delayed by ~ 5 time constants of the lock-in amplifier after each step of the moving mirror of the spectrometer.

For the SE studies the same measurement setup was used except for the lock-in amplifier. A pulsed optical pumping was used provided by either "SOLAR Laser Systems" KTP optical parametric oscillator emitting 10-ns-long pulses at 2 µm or CO_2 laser with 10.6 µm wavelength at 100-ns-long pulse. A repetition rate for both sources did not exceed 10 Hz, therefore the SE signal from the detector was acquired directly by external high-speed ADC triggered with the synchronization pulse as described in Ref[34].

3. PC kinetics study

The PC decay was measured after 7-ns-long narrow-band radiation pulses provided by the "SOLAR Laser Systems" optical parametric oscillator with the outcoming wavelength of 8.5 µm. The pulse energy was 10 µJ and the beam diameter on the sample was 7 mm. Using low-energy quanta for the excitation of PC was exploited to generate "cold" carriers in the vicinity of the k = 0 point so that the effects related to the carrier heating were avoided. The PC signal was acquired with a digital oscilloscope "Le Croy" with 1 GHz upper limiting frequency. Thus, the pulse duration limited the time resolution to ~7 ns. The details on the experimental setup can be found in Ref. [50].

Supplementary

Table I. Parameters of the structures under study: D_1 – thickness of the waveguide layer (grown on CdTe buffer from the substrate side, x_{wg}, x_{bar} – Cd content in waveguide layers and barriers, respectively (x-values are defined as in $Hg_{1-x}Cd_xTe$), d_{well} –thickness of QWs, E_g – bandgaps of structures calculated in the framework of Kane 8×8 model for T = 8K in units of cm^{-1} and SE wavelength at 8K.

Sample# label	D_{clad} (μm)	x_{wg}	x_{bar}	x_{QW}	d_{well} (nm)	E_g@8K calculated (cm^{-1})	SE wavelength @8K(μm)
S1(150120)	2	0.6±0.02	0.58±0.01	0±0.005	3.2	980	10.2
S2(170127)	5.2	0.6±0.02	0.66±0.01	0.8±0.01	7.4	660	14
S3(190419)	9	0.75±0.02	0.7±0.01	0.065±0.005	7.9	320	31
S4(190410)	9	0.71±0.02	0.61±0.02	0.073±0.005	7.4	410	23.6
S5(170130)	7.53	0.68±0.02	0.66±0.01	0.08±0.005	7.8	480	20.3
S6(161222)	8.1	0.65±0.02	0.63±0.02	0.102±0.01	6.1	890	10.9
S7(161222_1)	8.1	0.65±0.02	0.63±0.02	0.108±0.01	6.1	930	10.4

Figure Legends

Fig. 1 The suppression of Auger recombination for massive Dirac fermions. The left part of the figure shows an example of the interband (*e-h*) and intraband (*e-e*, *h-h*) carrier transitions within hyperbolic bands. The right part presents the loci of all possible interband (green areas) and intraband (red and blue areas) transitions in the phase space (*k, E*). Energy-momentum conversation laws require *e-h* vector be collinear with either *e-e* or *h-h* vector, which is not possible. No intersection occurs between the interband and the intraband transition loci, thus forbidding the AR.

Fig. 2 a The dynamics of the carrier density in structure S1 at 77K. The vertical axis is in natural logarithmic scale. The dashed line gives the calculated kinetics for RR with the initial carrier density 1.5×10^{11} cm^{-2}. **b** The reciprocal function of the experimental data with the offset subtracted and the corresponding exponential fit.

Fig. 3 The distribution of the refractive index (dashed lines) and TE$_0$ mode electric field (solid lines) in structure S3 for the wavelengths near 30 μm. Better confinement is evident for the wavelength of 31 μm, which is closer to the Reststrahlen band of the GaAs substrate.

Fig. 4 Band structure transformation in narrow gap HgCdTe layer sandwiched between Cd0.7Hg0.3Te barriers as the thickness of the layer is reduced from several microns to several nanometers.

Fig. 5 a Normalized temperature driven SE spectra for several structures under study. For structure S3 the PL spectrum is shown for comparison of the linewidths for PL and SE spectra; **b** The temperature of SE quenching T_{SEQ} vs. the threshold energy of Auger recombination E_{th} in HgCdTe QW structures. Labels give the longest SE wavelength obtained from the corresponding structure. The color of a dot corresponds to the energy spectrum of the same color presented in part e; **c** PL and SE spectra for structure S7 at 8K under continuous wave excitation at 900 nm. The legend gives the incident power in a 7-mm-diam spot; **d** SE integral signal vs. pumping intensity for several structures under study at different temperatures; **e** Valence band dispersion for several structures under study. The dashed lines indicate the "critical" hole energy corresponding to the threshold energy of AR.

Fig. 6 The dynamics of the carrier density in structure S5 at 77K. The vertical axis is in natural logarithmic scale. The dash-dot and dashed lines give the calculated kinetics for AR and RR, respectively, for initial carrier density 8.25×10^{10} cm^{-2}. The calculated kinetics of carrier density due to RR for a 5-nm-thick QW with the same bandgap as structure S5 is given in short dash curve.